MODELING AND ANALYSIS OF PV MODULE FAULTS IN GRID-CONNECTED SYSTEMS USING MATLAB/SIMULINK UNDER REAL WEATHER CONDITIONS

Beatriz Barbosa F. Ramos[1], Daniel Henrique N. Dias[1] and Alexandre de Arruda Bitencourt[1]

[1]Universidade Federal Fluminense (UFF), Niterói (Brazil)

Abstract

Photovoltaic (PV) systems have undergone rapid global expansion, accounting for a 30% increase in electricity generation by 2024 (IEA, 2025). Despite this growth, PV plants remain highly susceptible to performance degradation caused by harsh environmental conditions and insufficient maintenance, leading to electrical faults and reduced efficiency. This paper presents a detailed MATLAB/Simulink-based model developed to simulate and analyze fault behavior in a 150 kW grid-connected PV system under real meteorological conditions. To isolate the impact of DC-side disturbances, the inverter stage is modeled using ideal voltage sources, eliminating switching and control effects. Four representative fault scenarios were simulated to generate time-domain profiles of key electrical parameters, voltage, current, and power, enabling the identification of distinctive dynamic signatures for each fault type. The analysis provides insights into system response under abnormal conditions and supports the development of predictive maintenance and diagnostic strategies aimed at improving operational reliability and overall PV system performance.

Keywords: Photovoltaic fault diagnosis, Grid-connected PV systems, MATLAB/Simulink modeling, Fault analysis and simulation, Maximum power point tracking (MPPT).

1. Introduction

The rapid expansion of photovoltaic (PV) systems has positioned solar power as a central pillar of global decarbonization. However, PV modules remain susceptible to environmental stressors such as soiling, temperature fluctuations, and potential-induced degradation, leading to significant power losses and reduced reliability (IEA, 2022; Aghaei et al., 2022). Soiling alone can cause annual losses of 3-7%, highlighting the need for advanced monitoring and maintenance strategies.

Recent developments in Artificial Intelligence (AI) and data analytics have revolutionized PV fault detection, allowing predictive maintenance through anomaly recognition and performance trend analysis (Guan et al., 2024; Hadroug et al., 2025). Machine learning models, such as CNNs and XGBoost, achieve accuracies above 90% in identifying shading, degradation, or connection faults. At the same time, the analysis of current–voltage (I-V) and power-voltage (P-V) curves provides a complementary, non-invasive diagnostic approach for recognizing characteristic fault patterns (Huang et al., 2019; Lin et al., 2024).

Despite these advances, few studies combine detailed Simulink-based fault modeling with real meteorological inputs to produce datasets suitable for AI-based classification. This work addresses this gap by simulating multiple DC-side faults under real irradiance and temperature profiles, generating a structured fault behavior database for future diagnostic and predictive maintenance research.

2. Characterization of PV Faults

Faults in PV systems are defined as abnormal electrical conditions that reduce energy yield or compromise safety. They can be broadly classified as DC-side or AC-side faults, with the DC side being more critical due to its exposure to environmental factors and direct impact on power generation (Ghosh et al., 2018; Madeti & Singh, 2017; Khaled et al., 2023; Davarifar et al., 2013).

10.18086/swc.2025.03.44 Available at http://proceedings.ises.org

The present study focuses on four representative DC-side faults: short circuit, open circuit, partial shading, and degradation. Short circuits result from unintended low-impedance paths, leading to voltage collapse and potential overheating (Livera et al., 2018; Khaled et al., 2023). Open circuits, caused by disconnections or connector failures, interrupt the current path and isolate modules or strings. Partial shading produces mismatch losses and nonlinear I-V characteristics, while degradation gradually alters module resistances and efficiency (Kushwaha et al., 2023; Liu et al., 2021; Shaheen et al., 2023).

These faults were selected for their prevalence in field installations and their distinct dynamic signatures observable in both I-V and P-V curves. Figure 1 summarizes their classification and occurrence domains within the PV system. Among them, the fault types highlighted in gray, are those examined and discussed in detail in this paper.

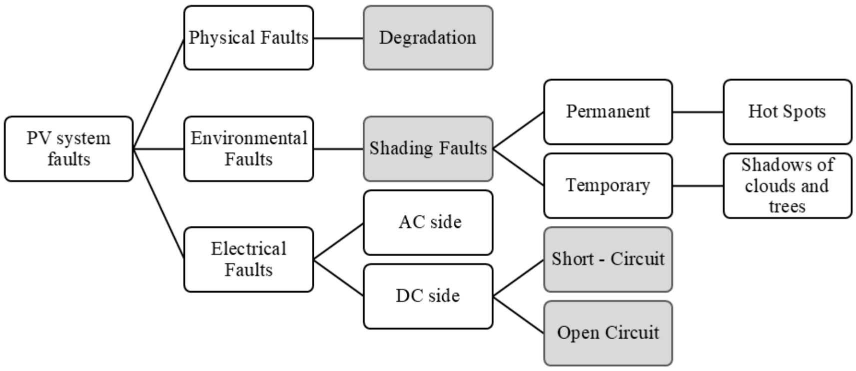

Figure 1: PV system faults.

3. Case Study and PV Plant Description

This study is based on the R&D project entitled "UFV Iguaba Grande: Universidade Federal Fluminense Living Lab for Open Innovation in the Solar Photovoltaic Industry", currently under implementation with financial support from FAPERJ (Fundação Carlos Chagas Filho de Amparo à Pesquisa do Estado do Rio de Janeiro).

The project aims to establish an experimental 1.0 MW grid-connected PV plant dedicated to applied research, performance evaluation of photovoltaic technologies, and the development of digital tools for intelligent operation and maintenance. The facility is being built on land owned by Universidade Federal Fluminense (UFF), located in the municipality of Iguaba Grande, in the Região dos Lagos of Rio de Janeiro State, Brazil. Once completed, it will serve as a "Living Laboratory" for open innovation, integrating academia, technological startups, and industry partners in the renewable energy sector.

The "UFV Iguaba Grande" plant adopts a modular configuration, designed to enable comparative analyses between distinct photovoltaic technologies and mounting topologies. The installation will consist of a central ground-mounted array of 400 kW complemented by four subsystems of 150 kW each, totaling 1.0 MW of installed capacity. Each subsystem includes five independent inverters (30 kW each), with five strings per inverter, allowing fine-grained monitoring and fault simulation.

Figure 2 presents an aerial view of the "UFV Iguaba Grande" facility currently under construction, showing the modular layout and distribution of the five subsystems. The experimental design combines monofacial and bifacial PV modules installed on both fixed-tilt and single-axis tracking structures. In tracking systems, the rotation axis is aligned north-south, enabling east–west movement to optimize solar capture throughout the day. The front face of the modules initially faces east, differing from conventional rooftop systems, which are generally north oriented.

This hybrid design allows comprehensive evaluation of the influence of structural and technological configurations on energy yield, efficiency, and reliability. In addition to energy performance monitoring, the plant will integrate thermal imaging via aerial infrared thermography, enabling automated fault detection and predictive maintenance through a dedicated asset management platform.

The "UFV Iguaba Grande" project adopts a multidisciplinary and open-innovation approach, combining field experimentation, numerical modeling, and artificial intelligence techniques. The insights and datasets generated will directly support the calibration and validation of computational models such as the one developed in this study, providing a replicable framework for intelligent fault diagnosis and data-driven management of large-scale PV plants.

Figure 2: Aerial view of the "UFV Iguaba Grande" PV plant under construction in Iguaba Grande, RJ.

4. Modeling and Simulation Framework

The proposed methodology is based on the computational modeling of the "UFV Iguaba Grande" PV plant in MATLAB/Simulink, developed to simulate its electrical behavior under different fault conditions. This environment enables detailed evaluation of PV module performance, inverter operation, MPPT control, and environmental interactions, providing a safe platform for testing fault diagnosis and control strategies before real-world deployment.

The simulated system represents one 150 kW subsystem of the UFV Iguaba Grande plant, composed of three 50 kW inverters, each connected to five independent PV strings, totaling 15 strings with 20 series-connected modules per string. Each string can operate under independently controlled irradiance, temperature, and fault parameters, allowing the isolation of specific fault effects at the string and inverter levels.

Figure 3(a) shows the electrical configuration of the simulated subsystem, comprising three inverter–array groups connected in parallel to a modeled three-phase grid. Figure 3(b) illustrates the transformation of the direct-axis current into the three-phase abc coordinate system using a Phase-Locked Loop (PLL) algorithm, implemented in the inverter control stage.

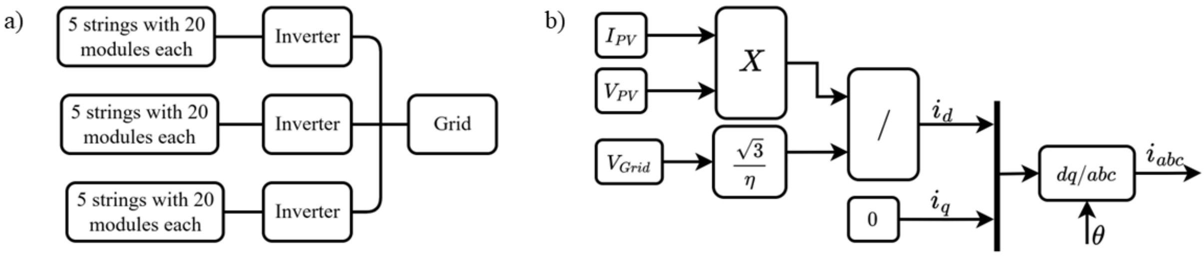

Figure 3: (a) Simulated subsystem "UFV Iguaba Grande". (b) Transformation of the direct-axis current into the abc coordinate system using a Phase-Locked Loop (PLL) algorithm in the inverter control stage.

4.1 PV Module Electrical Model

The electrical modeling of each PV module is based on the five-parameter single-diode model, widely adopted in the literature for its accuracy in reproducing the nonlinear current-voltage (I-V) characteristics of PV devices (Villalva et al., 2009). Each module is represented by a controlled current source, an ideal diode, a series resistance (R_s), and a shunt resistance (R_p), as illustrated in Figure 4(a). This configuration captures the main electrical losses and non-idealities that affect real PV operation.

The output current (I_m) of the PV module depends on both solar irradiance (G) and cell temperature (T), as described by Equations (1)-(3):

$$I_m = I_{pv} - I_0\left[\exp\left(\frac{V + R_s I}{a V_t}\right) - 1\right];\ V_t = \frac{N_s k T}{q} \text{ (Eq. 1)}$$

$$I_{pv} = \left(I_{pv,n} + k_i \Delta T\right)\frac{G}{G_n}\ ;\ \Delta T = T - T_n\ ;\ I_{pv,n} = \frac{Rp}{Rp + Rs} I_{sc,n} \text{ (Eq. 2)}$$

$$I_0 = \left(I_{sc,n} + K_i\,\Delta T\right)/\exp\left(\frac{V_{oc,n} + K_v\,\Delta T}{a V_t}\right) - 1 \text{ (Eq. 3)}$$

The model was implemented in MATLAB/Simulink using Simscape Electrical blocks, where each module is connected in series to form strings with the desired electrical characteristics. Figure 4 shows (a) the single-diode equivalent circuit and (b) its Simulink implementation.

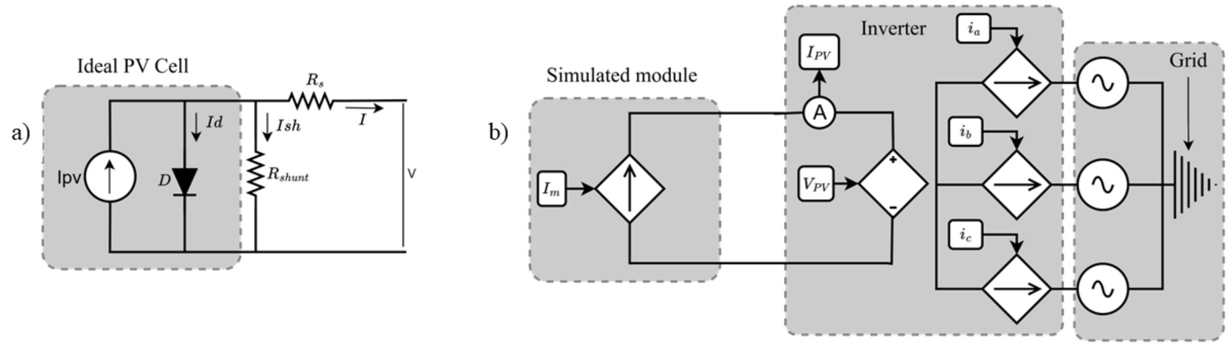

Figure 4: (a) Electrical modeling of the PV modules. (b) Implementation of the equivalent electrical model in MATLAB/Simulink

4.2 PV Equipment and Parameterization

For the simulated subsystem, Trina Solar Vertex 665W monofacial PV modules and Sineng Electric SN50/60PT inverters were selected. These commercial components define the electrical limits and operating window of the system, ensuring realistic power tracking and voltage range representation.

Key parameters, such as short-circuit current (I_{sc}), open-circuit voltage (V_{oc}), current and voltage at the maximum power point (I_{mpp}, V_{mpp}), number of series-connected cells (N_s), and temperature coefficients (K_i, K_v), were obtained directly from manufacturer datasheets.

To improve accuracy under non-ideal conditions (e.g., partial shading, temperature gradients, or degradation), initial estimates of series (R_s) and shunt (R_p) resistances were computed analytically based on deviations between the ideal and measured operating points, as shown in Equation (4) (Villalva et al., 2009):

$$R_s = \frac{V_{oc} - V_{mpp}}{I_{mpp}}\,;\ R_p = \frac{V_{mpp}}{I_{sc} - I_{mpp}} \quad \text{(Eq. 4)}$$

These parameters allow the model to capture mismatch losses and internal resistive effects consistent with real PV operation.

4.3 DC-Link Reference Voltage and String-Level Power Calculation

A key step in the modeling process is the definition of the reference voltage (V_{ref}) after the DC link. This voltage represents the steady-state potential that balances the total DC power and current from all strings connected to a given inverter. The reference voltage is computed dynamically from the simulated electrical quantities using:

$$V_{ref,i} = \frac{P_{total,i}}{I_{total,i}} \quad \text{(Eq. 5)}$$

Where:

1. $V_{ref,i}$ is the reference voltage for inverter i.
2. $P_{total,i} = \sum_{n=1}^{5} P_{pv,i,n}$ is total instantaneous power of the five strings (n).
3. $I_{total,i} = \sum_{n=1}^{5} I_{pv,i,n}$ is the corresponding total current of the five strings (n).

Each string operates under an independent MPPT controller, which determines its own best voltage and current based on local irradiance and temperature. This decentralized architecture enables accurate observation of fault propagation effects at both the string and inverter levels, avoiding electrical interference between parallel branches.

The current for each string ($I_{pv,i,n}$) is obtained directly from the single-diode model, while the instantaneous string power is computed as in Equation (6):

$$P_{pv,i,n} = V_{pv,i,n} \text{ x } I_{pv,i,n} \quad \text{(Eq. 6)}$$

Finally, the total DC power and current for each inverter are determined by Equation (7):

$$P_{total,i} = \sum_{n=1}^{5} P_{pv,i,n} \; ; \; I_{total,i} = \sum_{n=1}^{5} I_{pv,i,n} \quad \text{(Eq. 7)}$$

The independent MPPT configuration allows each string to autonomously regulate its DC-DC converter duty cycle, maximizing energy extraction even under irradiance mismatch, temperature variation, or localized faults. This design ensures that performance degradation in one string minimally affects the remaining ones, thereby preserving the overall system efficiency.

4.4 Inverter Modeling and Control Structure

The inverter was modeled in two distinct stages:

1. DC Side: Represented by an ideal voltage source, dynamically adjusted according to the V_{ref} value computed in Eq. (5), ensuring power balance at the DC bus and proper MPPT operation.
2. AC Side: The DC-AC conversion is performed by ideal current sources injecting power into a three-phase grid (230 V_{RMS} per phase), assuming a conversion efficiency of 95%. The direct-axis current component is transformed to a three-phase coordinate system using a Phase-Locked Loop (PLL) control, as illustrated in Figure 3(b).

Switching dynamics were neglected to reduce computational complexity, as the focus of this study lies in steady-state and fault condition analysis rather than converter switching behavior. This simplification is technically justified and does not compromise the accuracy of system-level evaluations.

4.5 Meteorological Data Integration and Fault Injection

Real irradiance and temperature data were obtained from the UFF Weather Station in Niterói (RJ, Brazil) for December 31, 2024, being a typical summer day. Each string receives its own G and T inputs, enabling simulation of non-uniform conditions such as partial shading and localized degradation.

Fault scenarios, including partial shading, degradation, short circuits, and open circuits, were simulated through a custom Graphical User Interface (GUI) developed in MATLAB, allowing users to configure the fault location, duration, and intensity in real-time.

All simulation data (voltage, current, and power) were automatically logged and exported to Excel for subsequent statistical analysis and machine-learning dataset generation.

4.6 Fault Modeling and Execution Strategy

Based on the previously established healthy state framework, the four fault types previously defined were simulated. Each fault condition was implemented through dedicated MATLAB scripts equipped with custom graphical user interfaces (GUIs) fully integrated into the simulation environment. These interfaces were developed to provide a user-friendly and flexible configuration process, allowing users to specify all relevant parameters associated with each fault event. Within the GUI, the user can select the target inverter (1-3), the affected string (1-5), and the exact time of fault occurrence, which is synchronized with the timestamps of the imported meteorological dataset. This integration ensures that every disturbance is applied under consistent irradiance and temperature conditions, maintaining comparability among scenarios.

For each simulation, the baseline configuration and meteorological inputs, irradiance, temperature, and temporal resolution, were kept constant to isolate the electrical effects of the faults from environmental variability. Once a fault is initiated, it remains active for the specified duration, typically persisting for the remainder of the simulated day. During this period, all relevant DC-side measurements (string voltage, current, and power) and AC-side parameters (RMS voltage and current at the grid interface) are continuously recorded. The resulting datasets are automatically stored in Excel files uniquely associated with each fault condition, allowing organized post-processing and direct comparison between healthy and faulty operation.

To ensure numerical stability and eliminate initial transients unrelated to the faulty events, data acquisition was programmed to begin after the first 301 simulation samples. This approach guarantees that all recorded responses correspond solely to steady-state behavior, providing reliable and reproducible electrical signatures for each fault type. The fault implementation methods are summarized as follows:

(A) Shading Fault

Shading was simulated by reducing the irradiance on selected strings using a user-defined shading factor, $F_{somb} \in [0, 1]$, applied via the GUI. The irradiance input was adjusted as follows:

$\mathrm{Irr_{somb}(i,j) = Irr_{orig}(i,j) \cdot (1 - F_{somb})}$ (Eq. 8)

Where $\mathrm{Irr_{somb}(i,j)}$ is the modified irradiance of string *j* in inverter *i*. The fault can emulate scenarios ranging from partial to complete obstruction of solar radiation, reproducing expected drops in current, power, and voltage.

(B) Degradation

Degradation was modeled in selected modules of inverter 1 by dynamically altering series and shunt resistances according to:

$\mathrm{R_s^{deg}(m) = R_s^{orig}(m).\,(1+F_{deg})}$ (Eq. 9)

$\mathrm{R_p^{deg}(m) = R_p^{orig}(m).\,(1 - F_{deg})}$ (Eq. 10)

Where $\mathrm{F_{deg}} \in [0,1]$ is the degradation factor defined by the user in the GUI, $\mathrm{R_s^{deg}(m)}$ and $\mathrm{R_p^{deg}(m)}$ are the degraded resistances of module ''m'', and $\mathrm{R_s^{orig}(m)}$ and $\mathrm{R_p^{orig}(m)}$ are their original values. Once the simulation is complete, original parameters are restored to preserve model integrity. This fault reduces module efficiency and induces asymmetries among strings.

(C) Short circuit

Short-circuit faults were modeled using a controlled ideal switch connected in parallel with the PV string output. During normal operation, the switch remains open, allowing the string to operate at its nominal maximum power point. At the fault instant, the switch closes, establishing a low-impedance path between the positive and negative terminals of the PV string, effectively reproducing a short-circuit condition.

To prevent numerical singularities and preserve solver convergence, a small series resistance ($R_{scr} = 1\times10^{-9}\ \Omega$) was inserted in series with the switch. This resistance limits the instantaneous current spike at the moment of fault inception while maintaining physically realistic short-circuit behavior. When the switch closes, the string voltage collapses nearly to zero, while the current rises toward the nominal short-circuit current (Isc). At the system level, this transient event can cause temporary voltage and current oscillations at the DC link, but independent MPPT controllers in the other strings stabilize the system rapidly after the disturbance.

(D) Open circuit

Open-circuit faults were simulated using an ideal switch connected in series with the PV string output. Under normal operation, the switch remains closed, allowing current to flow normally through the circuit. At the fault instant, the switch is opened, interrupting the current path and reproducing the electrical disconnection typical of an open-circuit condition (e.g., loose connectors or cable breakage).

To maintain numerical stability and avoid floating nodes during simulation, a high-value parallel resistance ($R_{par} = 1\times10^{9}\ \Omega$) was included across the switch terminals. This resistor ensures that the node voltage remains well-defined even when the switch is open, without introducing any significant leakage current. As a result, the string current drops nearly to zero, and the terminal voltage rises toward the open-circuit voltage (V_{oc}), representing the expected behavior of a disconnected PV string.

5. Results

The simulated results were obtained using the single-diode five-parameter model described in Section 4.1, parameterized with Trina Solar Vertex 665 W modules and Sineng 50 kW inverters. Figure 9 illustrates the electrical behavior of the PV system under a short-circuit fault applied to string 4 of inverter 1, initiated at 12pm and maintained until the end of the generation period. The inverter operates with five independent strings, each equipped with its own MPPT controller, allowing an isolated analysis of the fault's impact on both the affected string and the overall DC link.

Figure 9(a) shows the measured irradiance and temperature profiles for the analyzed day. The irradiance reaches a maximum of approximately 580 W/m² around noon, while the ambient temperature remains close to 31 °C throughout the period. These stable conditions ensure that the variations observed in the electrical quantities are due solely to the fault occurrence.

Figure 9(b), the DC link power under healthy operation (red curve) follows the irradiance trend, reaching a maximum of approximately 22-23 kW. When the short-circuit fault occurs, the power of String 4 (green dashed line) collapses completely, indicating the creation of a low-impedance path through the controlled ideal switch.

Consequently, the DC link power (black dashed line) decreases significantly but not completely, as the other strings maintain normal operation.

Notably, small transient oscillations, or power ripples, appear in the waveform at once after the fault is triggered. These oscillations correspond to the MPPT controller's adaptive response, in which the Perturb and Observe (P&O) algorithm continuously perturbs the operating point in search of a new MPP (Esram & Chapman, 2007; Ghasemi et al., 2018; Hohm & Ropp, 2003). During the fault transition, the algorithm momentarily oscillates between high and low duty cycles, producing the observed ripples in both power and current. Once the MPPT stabilizes under the new fault condition, the oscillations attenuate.

Figure 9(c) presents the voltage behavior. Before the fault, String 4 operates near 800 V, corresponding to the nominal MPP voltage. Upon fault activation, the string voltage drops sharply to nearly 0 V, as the switch establishes a short path through a series resistor of 1×10^{-9} Ω. The DC link voltage shows only a slight dip and quickly stabilizes due to the autonomous action of the other MPPTs.

Figure 9(d) displays the current behavior. Before the fault, the total DC link current reaches approximately 32 A. After fault initiation, the current in String 4 briefly spikes and then settles near the short-circuit current (I_{sc}) due to the near-zero terminal voltage, while string power collapses to approximately 0 W. The total DC link current decreases modestly, consistent with the loss of one string, while minor oscillations appear during the fault transition, again reflecting the MPPT's transient re-adaptation to the new system impedance.

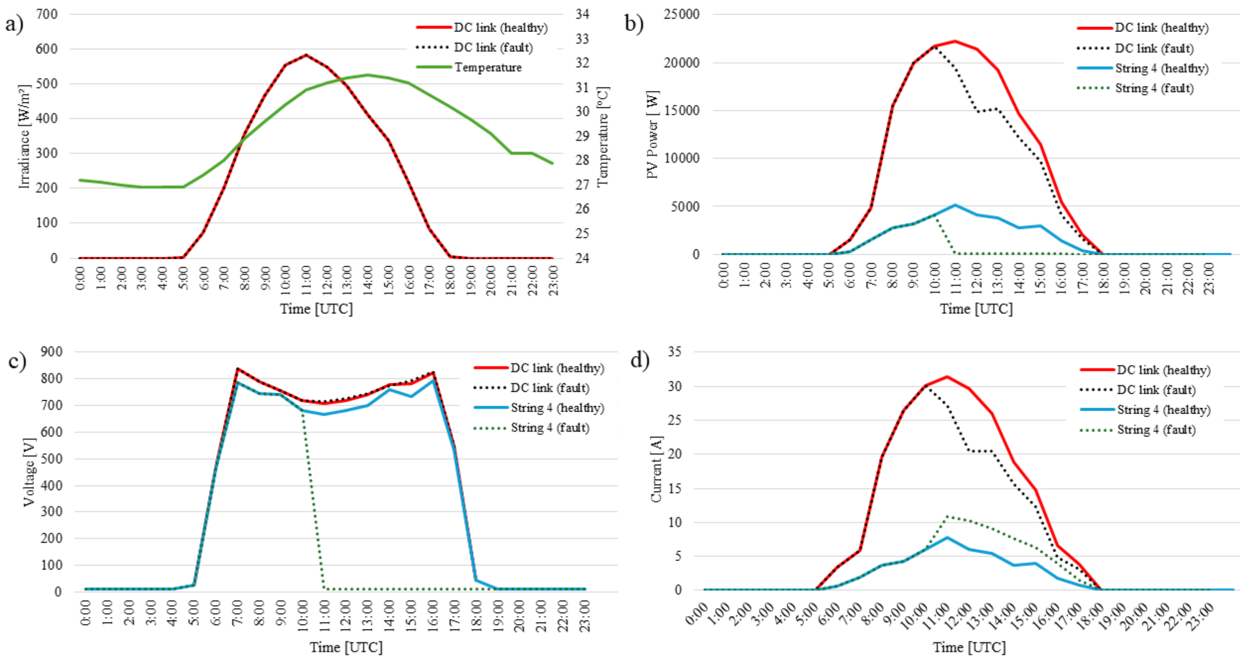

Figure 9: Comparison between healthy and short-circuit operating states. (a) Irradiance and temperature; (b) DC power; (c) Voltage; (d) Current for string 4 of inverter 1.

Figure 10 illustrates the system response under an open-circuit fault applied to String 3 of inverter 1, initiated at 12pm and maintained until the end of the generation period.

Figure 10(a) presents the irradiance and temperature profiles. The irradiance reaches its peak of about 600 W/m², while the temperature remains stable near 30 °C, ensuring that the electrical variations originate exclusively from the fault condition.

Figure 10(b), the DC link power under healthy operation (red line) peaks around 23 kW. When the open-circuit fault occurs, the power of String 3 (green dashed line) abruptly drops to zero, confirming the interruption of the current path. The DC link power (black dashed line) decreases by approximately 20%, corresponding to the loss of one out of five strings. Similar to the short-circuit event, small transient oscillations, also known as power ripples, appear at once after the fault initiation due to the MPPT perturbation cycle, as discussed by Esram & Chapman, 2007 and Ghasemi et al., 2018. These oscillations arise from the transient instability of the P&O algorithm, which attempts to re-locate the new MPP following the sudden impedance increase caused by the high-resistance path (1×10^{9} Ω) of the open switch (Hohm & Ropp, 2003; Femia et al., 2005). As the controller does not detect a valid operating point in the disconnected string, it momentarily oscillates between control limits before stabilizing at zero power.

Figure 10(c) shows the voltage behavior. Before the fault, the string operates approximately 770 - 780 V, consistent with normal MPP conditions. After the switch opens, the high-impedance path prevents current flow, causing the voltage to rise toward V_{oc} (≈ 800 V). The DC link voltage remains steady, reflecting the isolation provided by the independent MPPTs.

Figure 10(d) illustrates the current behavior. When the open-circuit fault occurs, the string current (green dashed line) at once drops to zero, while the currents of the healthy strings remain unaffected. Small oscillations are observed in both string and DC link currents at once after the fault. These oscillations result from the MPPT algorithm's transient perturbation and its delayed recognition of the disconnection, leading to brief control fluctuations before stabilization. Afterward, the current and power curves settle to steady-state zero for the faulted branch.

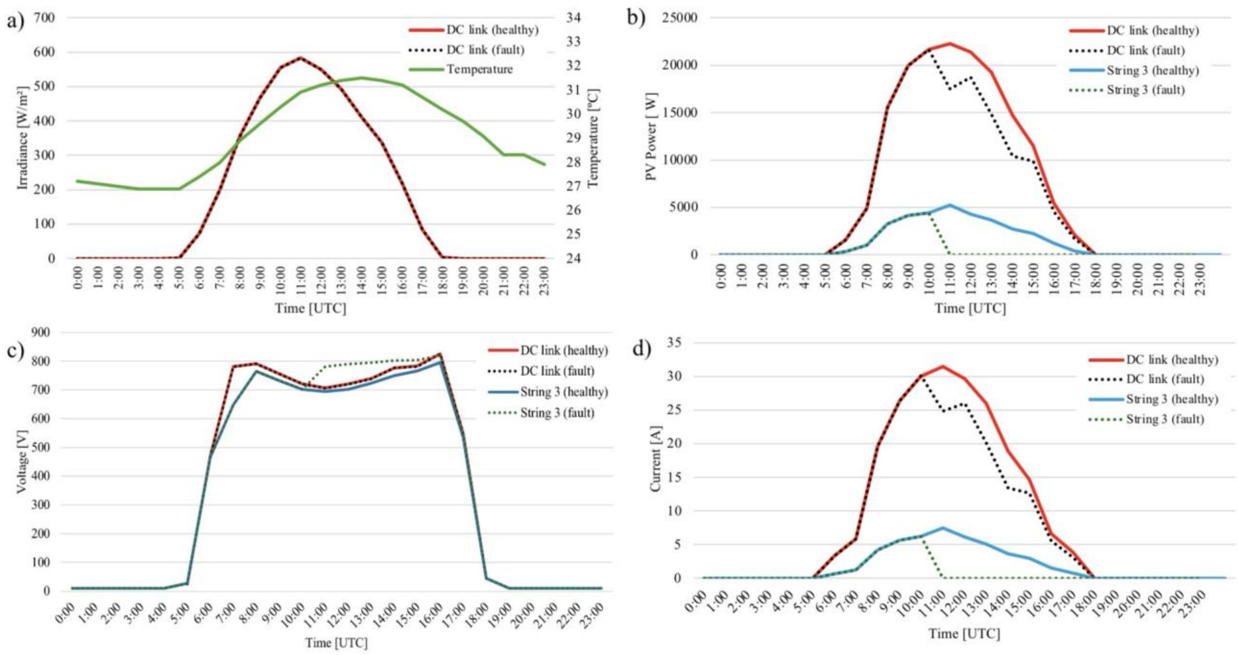

Figure 10: Comparison between healthy and open-circuit operating states. (a) Irradiance and temperature; (b) DC power; (c) Voltage; (d) Current for string 3 of inverter 1.

Figure 11 illustrates the effects of a partial shading event affecting 80% of the PV modules in string 2 of inverter 1, occurring in two steps: 9 and 11am; 2 and 3pm. This fault simulates the passage of dense clouds over a part of the PV array, producing a temporary and non-destructive disturbance.

Figure 11(a) shows the irradiance and temperature profiles, where two distinct irradiance dips can be observed, corresponding to the shading intervals. The temperature remains stable, ensuring that the electrical variations are solely due to irradiance reduction.

Figure 11(b) displays the power response. During shading periods, the power of string 1 (blue dotted curve) decreases, following the irradiance profile. The total DC link power (black dotted) also exhibits a moderate drop, proportional to the reduction in available power from the shaded string. The independent MPPT controller of string 1 autonomously adjusts its operating point to a new maximum power point (MPP) at a lower voltage and power level, while the remaining strings continue normal operation, supporting stability (Esram & Chapman, 2007; Ghasemi et al., 2018).

Figure 11(c) shows the voltage response. The voltage of the shaded string temporarily decreases, consistent with the shift of the MPP toward lower voltages under reduced irradiance. The DC link voltage experiences minor fluctuations without instability, confirming the robustness of the control system. Once the irradiance returns to normal, both voltage and power quickly recover to their nominal values.

Figure 11(d), the current of string 1 drops significantly during the shaded periods, while the total DC link current exhibits smaller variations, as the unaffected strings partially compensate for the power loss. After the shading event, both currents recover at once, confirming the dynamic responsiveness of the P&O MPPT algorithm (Hohm & Ropp, 2003; Femia et al., 2005; Killi & Samanta, 2015).

Overall, the results confirm that independent MPPT operation effectively mitigates the impact of partial shading on system performance, ensuring stable DC link operation and fast recovery after transient irradiance disturbances.

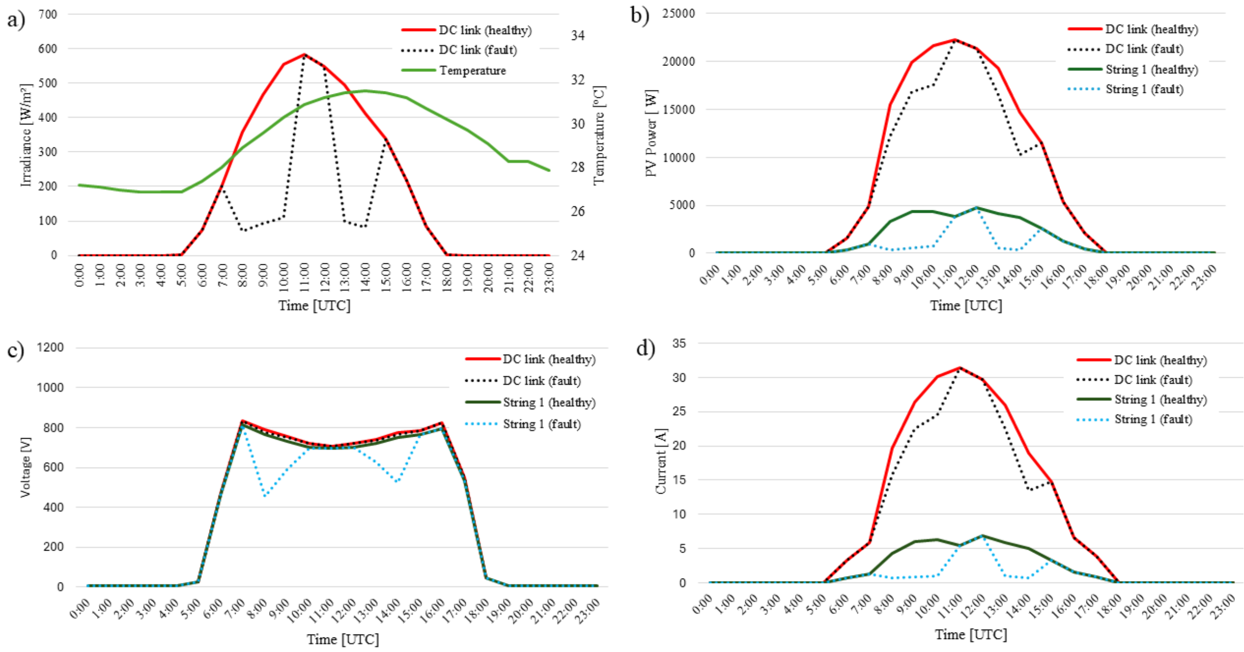

Figure 11: Comparison between healthy and partial shading faults. (a) Irradiance and temperature; (b) DC power; (c) Voltage; (d) Current for string 2 of inverter 1.

Figure 12 presents the behavior of the system under a severe degradation condition applied to all modules of string 1 in inverter 1, reducing their efficiency by 70% throughout the entire generation period. Unlike the abrupt short-circuit and open-circuit faults, degradation represents a continuous and permanent process of performance loss in PV modules, typically caused by material aging, microcracks, or environmental stress.

Figure 12(a) presents the irradiance and temperature profiles for the simulation day. In Figure 12(b), the power of the degraded string (blue dotted curve) is substantially lower than that of the healthy string (green line) across the entire day. The DC link power (black dotted curve) also decreases proportionally, reflecting the permanent loss of energy contribution from the degraded string.

Figure 12(c) reveals that the voltage of the degraded string 2 is slightly higher than that of the healthy string. Although this might appear counterintuitive, it is consistent with the expected behavior under severe degradation when operating with independent MPPTs. As the photogenerated current decreases drastically, the MPPT controller of the degraded string shifts its operating point toward a higher-voltage and lower-current region, close to the open-circuit voltage (Voc). Since the degraded string contributes little current to the overall DC link, its voltage remains nearly decoupled from the others, operating autonomously according to its MPPT algorithm.

Figure 12(d) shows that the current of the degraded string remains at about 30% of its nominal value, consistent with the applied degradation factor. The total DC link current experiences a modest reduction but remains stable throughout the entire day, indicating that the system maintains normal operation despite the significant degradation in one string.

This behavior confirms that severe degradation reduces current generation, thereby shifting the MPP toward higher voltages. The system remains stable, and the P&O MPPT algorithm successfully maintains the maximum available power under degraded conditions, demonstrating robustness and control reliability (Hohm & Ropp, 2003; Femia et al., 2005).

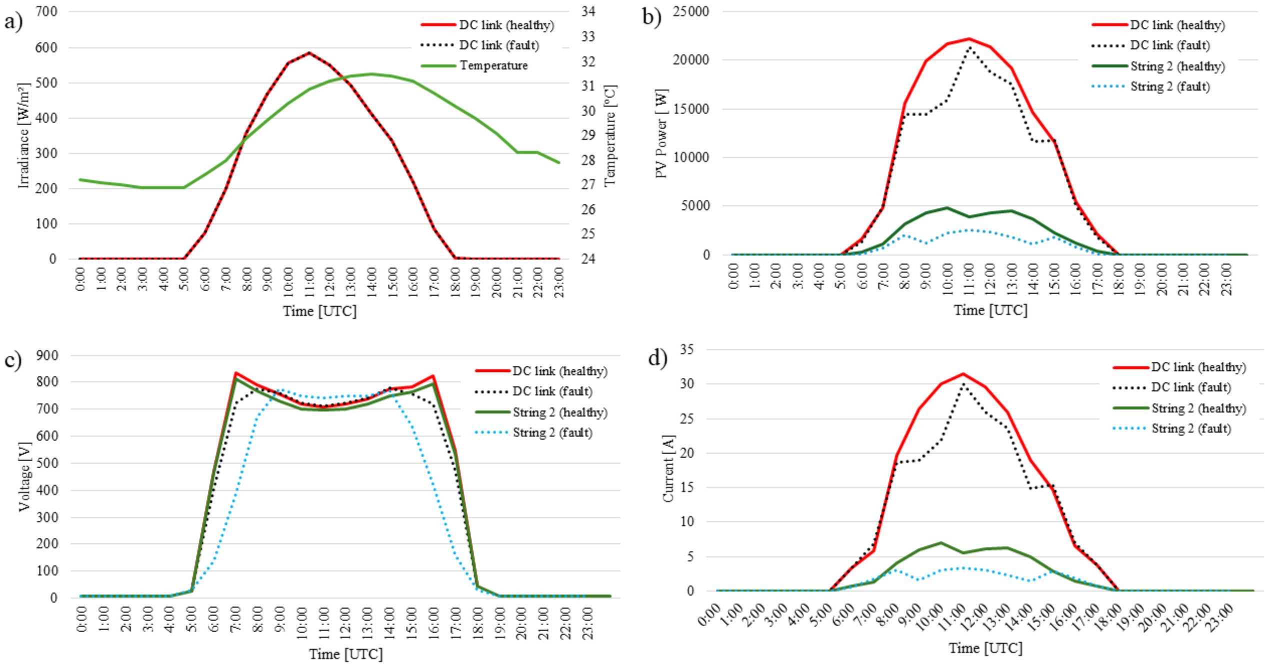

Figure 12: Comparison between healthy and degraded operating states. (a) Irradiance and temperature; (b) DC power; (c) Voltage; (d) Current for string 1 of inverter 1.

6. Conclusion

This study presented a comprehensive modeling and analysis framework for evaluating fault scenarios in grid-connected photovoltaic (PV) systems using the MATLAB/Simulink environment under real meteorological conditions. The proposed methodology integrated irradiance and temperature data obtained from the UFF weather station in Niterói, Brazil, corresponding to a typical summer day (December 31, 2024). By embedding these real environmental profiles into the customized “UFV_Iguaba” model, the system’s dynamic response was assessed with high temporal resolution under both healthy and faulty operating conditions.

Four representative fault types were investigated: partial shading, degradation, short circuit, and open circuit, each applied to specific strings of inverter 1. A user-friendly graphical interface was developed to control the location, intensity, and timing of each fault, enabling the simulation of realistic operational disturbances frequently observed in field-deployed PV systems.

The simulation results revealed distinct electrical signatures for each fault type in key system variables such as DC power, voltage, and current, while irradiance remained constant for electrically induced faults. Partial shading produced nonlinear MPPT behavior and mismatch losses; degradation caused a continuous reduction in performance throughout the day due to altered electrical characteristics; short-circuit faults resulted in voltage collapse and dissipative current paths; and open-circuit faults led to complete current interruption accompanied by a drop in power and voltage levels. Importantly, all faults remained electrically isolated at the string level owing to the independent MPPT architecture, ensuring stable operation of unaffected strings.

The proposed modeling framework proved effective in reproducing realistic dynamic responses to different fault conditions and demonstrated the importance of high-resolution, string-level monitoring for fault diagnosis and system reliability assessment. These findings highlight the framework’s potential to support the development of intelligent fault detection algorithms, predictive maintenance strategies, and design optimization tools for large-scale PV installations.

Future research will focus on extending this approach through the integration of Machine Learning based fault classification techniques, the inclusion of long-term meteorological datasets, and experimental validation using real field measurements. Overall, the methodology established in this work provides a reliable, flexible, and scalable platform for advanced analysis of PV system performance and reliability under real-world operating conditions.

7. References

Aghaei, M. et al. (2022) Review of degradation and failure phenomena in photovoltaic modules: A state-of-the-art overview. Renewable and Sustainable Energy Reviews, 162, 112440. https://doi.org/10.1016/j.rser.2022.112440

Davarifar, M., Rabiee, A. & Mohammadi, S. (2013) Comprehensive modulation and classification of faults in the DC side of PV systems. Energy and Power Engineering, 5(4), 230–236. https://doi.org/10.4236/epe.2013.54031

Esram, T. & Chapman, P.L. (2007) Comparison of photovoltaic array maximum power point tracking techniques. IEEE Transactions on Energy Conversion, 22(2), 439–449. https://doi.org/10.1109/TEC.2006.874230

Femia, N., Petrone, G., Spagnuolo, G. & Vitelli, M. (2005) Optimization of perturb and observe maximum power point tracking method. IEEE Transactions on Power Electronics, 20(4), 963–973. https://doi.org/10.1109/TPEL.2005.850975

Ghasemi, M.A., Foroushani, H.M. & Parniani, M. (2018) Partial shading detection and smooth maximum power point tracking of photovoltaic arrays under PSC. arXiv preprint arXiv:1803.09036. Available at: https://arxiv.org/abs/1803.09036

Ghosh, R., Das, S. & Pradhan, C.K. (2018) Classification of different types of faults in a PV system. In: IEEE International Conference on Computation of Power, Energy, Information and Communication (ICCPEIC). pp. 1–6. https://doi.org/10.1109/ICCPEIC.2018.8525230

Guan, J., Zhang, X., Liu, F. & Li, Y. (2024) Development of intelligent fault diagnosis and predictive maintenance algorithm in photovoltaic power generation systems. In: IEEE Power, Energy and Environment Conference (PEEEC). pp. 112–118. https://doi.org/10.1109/PEEEC58618.2024.10329524

Hadroug, N., Boulahlib, M., Bensaid, S. & Saidi, A. (2025) Practical implementation based on histogram of oriented gradient descriptor combined with deep learning. Journal of Industrial Information Integration, 35, 101880. https://doi.org/10.1016/j.jii.2024.101880

Hohm, D.P. & Ropp, M.E. (2003) Comparative study of maximum power point tracking algorithms. Progress in Photovoltaics: Research and Applications, 11(1), 47–62. https://doi.org/10.1002/pip.459

Huang, J.M., Chen, Y. & Lin, C.H. (2019) Fault diagnostic method for solar PV generation systems based on I–V curve measurement. IEEE Transactions on Industry Applications, 55(6), 5896–5905. https://doi.org/10.1109/TIA.2019.2930507

International Energy Agency (IEA) (2022) Soiling losses: Impact on the performance of photovoltaic power plants. Paris: IEA Publications. Available at: https://iea-pvps.org

International Energy Agency (IEA) (2025) Renewables 2025 – Market Update. Paris: IEA Publications. Available at: https://www.iea.org/reports/renewables-2025

Killi, M. & Samanta, S. (2015) Modified perturb and observe MPPT algorithm for drift avoidance in photovoltaic systems. IEEE Transactions on Industrial Electronics, 62(9), 5549–5559. https://doi.org/10.1109/TIE.2015.2408773

Khaled, O., Ahmad, S., Bashir, S. & Memon, M. (2023) A critical review of PV systems' faults with relevant detection methods. Energy Nexus, 10, 100152. https://doi.org/10.1016/j.nexus.2023.100152

Kushwaha, N., Singh, V. & Sharma, R. (2023) Effect of partial shading on PV system performance and mitigation techniques – A review. Energy Sources, Part A: Recovery, Utilization, and Environmental Effects, 45(10), 1861–1875. https://doi.org/10.1080/15567036.2022.2036822

Lin, W.T., Chang, H.C. & Chen, J.Y. (2024) Fault diagnosis in solar array I–V curves using characteristic simulation and multi-input models. Applied Sciences, 14(13), 5417. https://doi.org/10.3390/app14135417

Liu, J., Zhang, W., Chen, Z. & Wang, H. (2021) Degradation mechanisms and partial shading of glass-backsheet and double-glass PV modules. Solar Energy, 224, 1291–1301. https://doi.org/10.1016/j.solener.2021.06.022

Livera, A., Kotsampopoulos, P. & Hatziargyriou, N. (2018) Failure diagnosis of short- and open-circuit fault conditions in PV systems. In: IEEE World Conference on Photovoltaic Energy Conversion (WCPEC). pp. 2108–2113. https://doi.org/10.1109/PVSC.2018.8547563

Madeti, S.R. & Singh, S.N. (2017) A comprehensive study on different types of faults and detection techniques for solar PV systems. Solar Energy, 158, 161–185. https://doi.org/10.1016/j.solener.2017.08.069

Shaheen, E., Ali, R. & Hassan, K. (2023) Fault detection of partial shading faults in solar PV energy systems. In: IEEE International Conference on Electronic Engineering (ICEE). pp. 312–317. https://doi.org/10.1109/ICEE59396.2023.10129361

Villalva, M.G., Gazoli, J.R. & Filho, E.R. (2009) Comprehensive approach to modeling and simulation of photovoltaic arrays. IEEE Transactions on Power Electronics, 24(5), 1198–1208. https://doi.org/10.1109/TPEL.2009.2013862